Article:

Flow of non-Newtonian fluids in fractured porous media: Isogeometric vs standard finite element discretisation

Tim Hageman | René de Borst*

Department of Civil and Structural Engineering, University of Sheffield, Sheffield, UK

Correspondence
*René de Borst, Department of Civil and Structural Engineering, University of Sheffield, Sheffield S1 3JD, UK. Email: r.deborst@sheffield.ac.uk

Summary

A formulation has been derived for the flow of non-Newtonian (power-law) fluids in deformable, fractured porous media. The formulation is enhanced with a sub-grid scale model to accurately represent the flow of the power-law fluids inside the cracks. The resulting equations have been discretised using standard (Lagrangian) finite element shape functions as well as with Non-Uniform Rational B-Splines (NURBS), which have been cast into a standard finite element datastructure using Bézier extraction. The effect of the power-law index on the velocity inside the fracture and on the total fluid flow through the porous medium has been analysed for a typical boundary-value problem. It is shown that large differences between non-Newtonian and linearised Newtonian fluids can occur for the fluid velocity inside the fracture. This can significantly influence the total fluid transport through the domain. A mesh sensitivity study has been carried out as well, and shows that markedly smaller element sizes are required in order to obtain accurate results for the local flow inside the fracture, compared to the element sizes necessary for obtaining accurate results inside the porous medium away from the fracture. Moreover, a comparison has been made between the results obtained using standard Lagrange polynomials and those obtained using NURBS. It is shown that while both discretisation methods are able to accurately simulate the deformations and pressures in the porous medium, the higher interelement continuity of NURBS is mandatory for obtaining correct values of the fluid velocities inside the fracture, especially near the tips.

KEYWORDS:
poroelasticity, fracture, non-Newtonian fluids, power-law fluids, isogeometric analysis

1 | INTRODUCTION

Fluid flow in porous media is of major importance for a large number of geomechanical problems. Examples are underground oil flow and recovery, and the spreading of pollutants. Applications outside geo-engineering include blood flow, and fluid flow through filters. In most cases, the flow field is not only influenced by the properties of the fluid and the microstructure of the porous medium, but also by the possible presence of fractures, either pre-existing, or induced.

In one of the early models for simulating flow and deformation in fractured or fracturing porous media, the continuum was discretised using finite elements, while the fluid flow inside the (single) fracture was approximated using a finite difference method [1]. Alternatively, the use of zero-thickness hydromechanical interface elements has been suggested, initially for modelling

fluid-filled pre-existing fractures[2,3]. For propagating cracks remeshing can be used, where hydromechanical interface elements are still used for modelling the flow in the fracture[4,5]. Alternatively, extended finite elements can be used to model pre-existing fractures as well as freely propagating fractures[6] or shear bands[7].

Different from the approach pioneered by Boone and Ingraffea[1], where the porous continuum and the crack were modelled as different domains, a multi-scale approach can be adopted which builds on the observation that the width of the crack is several orders of magnitude smaller than its in-plane dimensions or the dimensions of the porous bulk material. The advantage is that an extra mesh to simulate the fluid flow inside the fractures is not required. Yet, it allows to simulate the effects of fractures on the fluid flow while keeping a relatively coarse mesh, thus enabling the simulation of large domains. This assumption was used in zero-thickness hydro-mechanical interface elements, either for pre-existing faults[2,3], or for propagating cracks using remeshing techniques[4,5]. A subgrid scale model to capture the fluid flow in the fracture has been formulated departing from the assumption that the in-plane dimensions of the fracture are large compared to its width[8]. Unsurprisingly, the result is an expression closely related to Reynolds' equation, including the cubic dependence on the fracture width. However, since the approach assumes the fluid pressures in the crack and in the bulk material to be equal, leak-off, as for instance encountered when pressurising a crack (e.g., in hydraulic fracturing), cannot be modelled. To enable the inclusion of a pressure difference in the formulation by using an interface permeability, a generalised subgrid scale was introduced[9,10,11]. A different approach to represent the added fluid transport inside the fractures was published by Khoei and co-workers[12,13,14].

A further complication is that in relevant applications the fluid behaviour is often non-Newtonian. This requires the problem either to be approximated, to be linearised, or to have the nonlinear effects included in the formulation. Not much work been done on the flow of non-Newtonian fluids in porous media[15,16], or on the modelling of non-Newtonian fluid flow inside pressurised fractures[17]. Yet, the potential impact of including non-Newtonian fluid flow on the propagation speed and direction of fractures has been demonstrated[18]. Further simulations of non-Newtonian fluids in porous media with pre-existing cracks, albeit restricted to non-deformable porous media, have shown the influence of these cracks on the pressure gradient, which in turn influences the behaviour of the fluid inside the porous medium[19].

While many applications involve non-Newtonian fluids and the effects can be important, no formulations exist for a deformable, poroelastic medium, including the effect of the fluid transport inside fractures. The aim of this paper is to present a formulation which encompasses these effects. In this contribution the flow inside the porous medium will be approximated using the generalised Darcy law[20]. The flow inside the cracks will be simulated using a subgrid scale, continuous pressure model, where the fluid pressure is assumed to be continuous across the crack, similar to the formulation for Newtonian fluids[8]. The influence of the power-law index on the behaviour of the fluid inside the poroelastic bulk material and inside the fracture will be analysed, and we will show the influence of including the non-Newtonian effects compared to linearising the fluid and approximating it as Newtonian. Attention will also be given to mesh sensitivity, and we will show the difference between using isogeometric shape functions compared to traditional Lagrangian shape functions.

2 | GOVERNING EQUATIONS

We consider a domain Ω which consists of a porous material and is divided into two parts by a discontinuity Γ_d, Figure 1. To represent a crack Γ_d must be C^{-1} discontinuous in the displacements. For modelling the fluid pressure across the discontinuity, various possibilities exist[10,11]. The simplest possibility, which has been adopted here, is to assume that the pressure is C^0 continuous at Γ_d, which implies that the velocity of the fluid is discontinuous across Γ_d.

2.1 | The porous bulk material

We consider quasi-static processes and assume that the deformations in the solid occur fast compared to the fluid flow. These assumptions allow a description of the domain Ω by the hydro-static momentum balance:

$$\nabla \cdot \boldsymbol{\sigma} = \mathbf{0} \qquad \boldsymbol{x} \in \Omega \tag{1a}$$

$$\boldsymbol{u} = \overline{\boldsymbol{u}} \qquad \boldsymbol{x} \in \Gamma_u \tag{1b}$$

$$\boldsymbol{n} \cdot \boldsymbol{\sigma} = \overline{\boldsymbol{t}} \qquad \boldsymbol{x} \in \Gamma_t \tag{1c}$$

$$\boldsymbol{n}_d \cdot \boldsymbol{\sigma} = \boldsymbol{t}_{\Gamma_d} \qquad \boldsymbol{x} \in \Gamma_d \tag{1d}$$
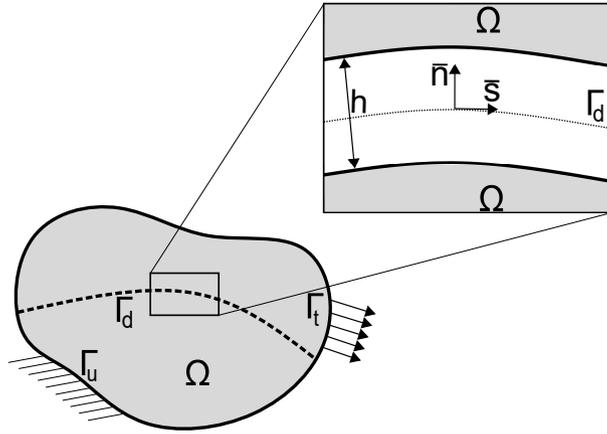
FIGURE 1 Schematic overview of the domain Ω with the internal discontinuity Γ_d. The local coordinate system $\overline{s}, \overline{n}$ is used for the fracture, and h is the fracture height.

with u the displacements of the porous material, $\overline{u}$ the prescribed displacements on the boundary Γ_u, while $\overline{t}$ and t_{Γ_d} are the tractions on the external boundary Γ_t and the internal discontinuity Γ_d, respectively. n is the normal vector of Γ_t, and n_d that of the discontinuity, Γ_d.

The total stress σ in a fully saturated porous material is defined as:

$$\sigma = \sigma_s - \alpha p I \tag{2}$$

where I is the second-order unit tensor, α is the Biot coefficient, and p the pressure of the interstitial fluid in the porous material. The stress inside the solid material, σ_s, is assumed to be linearly related to the strain via:

$$\sigma_s = D : \varepsilon \tag{3}$$

with D the elastic fourth-order stiffness tensor of the porous material and $\varepsilon = \nabla^s u$ the infinitesimal strain of the porous material, ∇^s denoting the symmetrised gradient operator.

The fluid pressure is obtained from the mass conservation of the solid and fluid subject to the appropriate boundary conditions:

$$\frac{1}{M} \frac{\partial p}{\partial t} + \alpha \nabla \cdot \dot{u} + \nabla \cdot q = 0 \qquad x \in \Omega \tag{4a}$$

$$p = \overline{p} \qquad x \in \Gamma_p \tag{4b}$$

$$n \cdot q = \overline{q} \qquad x \in \Gamma_q \tag{4c}$$

$$n_d \cdot q = n_d \cdot q_d \qquad x \in \Gamma_d \tag{4d}$$

with p being the pressure of the interstitial fluid, $q = n_f(v - \dot{u})$ the flux of the fluid within the porous material, and $\dot{u}$ and v being the velocities of the solid and fluid, respectively, n_f is the porosity, $\overline{p}$ the prescribed pressure on Γ_p, $\overline{q}$ the prescribed inflows on Γ_q, q_d the fracture inflow on Γ_d and M the Biot modulus.

Within non-Newtonian fluids the power law model is the most widely used. In it, the shear stress is defined as:

$$\tau = \mu_0 \left(\frac{\partial v}{\partial y} \right)^n \tag{5}$$

with μ_0 the consistency factor or base viscosity and $\frac{\partial v}{\partial y}$ the shear rate in the fluid. n is the power-law fluid index with $n < 1$ representing shear-thinning fluids, $n = 1$ defining Newtonian fluids, and $n > 1$ for shear-thickening fluids. In a one-dimensional context the fluid flux of power-law fluids inside porous media can be cast in the following explicit format [20,21,22]:

$$q = k_f^* \left(\frac{\Delta p}{\Delta L} \right)^{\frac{1}{n}} \tag{6}$$

with Δp a pressure difference applied over a distance ΔL. The effective permeability k_f^* is defined as:

$$k_f^* = \frac{n}{3n+1} \left(\frac{50}{3} k \right)^{\frac{1+n}{2n}} (2C\mu_0)^{-\frac{1}{n}} n_f^{\frac{n-1}{2n}} \tag{7}$$

with k the intrinsic permeability of the porous material and C a constant normally taken as $\frac{50}{24}$ [22]. Since k_f^* only depends on material properties of the solid and the fluid, its value is constant. An implicit form for multi-dimensional cases has been formulated and used as well [23,15]:

$$\nabla p = -\frac{\mu_0}{k^*} |\boldsymbol{q}|^{n-1} \boldsymbol{q} \tag{8}$$

with k^* defined as:

$$k^* = \frac{1}{2C} \left(\frac{50k}{3n_f} \right)^{\frac{n+1}{2}} \left(\frac{n \, n_f}{3n+1} \right)^n \tag{9}$$

Equation 8 can be rewritten in an explicit format:

$$\boldsymbol{q} = -k_f^* |\nabla p|^{\sum_{i=1}^{\infty}(1-n)^i} \nabla p \tag{10}$$

Assuming $0 < n < 2$, which is valid for most fluids, this equation can be simplified to [24]:

$$\boldsymbol{q} = -k_f^* |\nabla p|^{\frac{1}{n}-1} \nabla p \tag{11}$$

Finally, the conservation of mass as in equation 4a is combined with the explicit expression for the flux of the power-law fluid (equation 11), which results in:

$$\frac{1}{M} \frac{\partial p}{\partial t} = -\alpha \nabla \cdot \dot{\boldsymbol{u}} + k_f^* \nabla \cdot \left(|\nabla p|^{\frac{1}{n}-1} \nabla p \right) \tag{12}$$

2.2 | Fluid-transporting fractures

The traction at the internal discontinuity, $\boldsymbol{t}_{\Gamma_d}$, is assumed to be composed of an effective traction, $\boldsymbol{t}_d$ and the fluid pressure p acting on the walls, similar to the decomposition of the total stress in the bulk material, eq. 2:

$$\boldsymbol{t}_{\Gamma_d} = \boldsymbol{t}_d - p\boldsymbol{n}_d \tag{13}$$

The traction $\boldsymbol{t}_d$ can be obtained from a cohesive-zone model [25], but in the examples shown has been assumed zero ($\boldsymbol{t}_d = \boldsymbol{0}$) for the complete fracture. To solve the equations in an incremental-iterative manner, eq. 13 needs to be linearised. Noting that the traction is a function of the crack opening $[\![\boldsymbol{u}]\!]$ the result is:

$$d\boldsymbol{t}_{\Gamma_d} = \boldsymbol{D}_d d[\![\boldsymbol{u}]\!] - \boldsymbol{n}_d dp \tag{14}$$

with the stiffness matrix:

$$\boldsymbol{D}_d = \frac{\partial \boldsymbol{t}_d}{\partial [\![\boldsymbol{u}]\!]} \tag{15}$$

Zero-thickness hydromechanical interface elements were used to model the initial crack, but also inserted for the crack extension a priori. In order to prevent adding a nonphysical compliance to these non-fractured elements, the stiffness matrix is then given by:

$$\boldsymbol{D}_d = \begin{bmatrix} k_n & 0 \\ 0 & k_s \end{bmatrix} \tag{16}$$

with the dummy stiffness parameters k_n and k_s being assigned high values. Since the traction - crack-opening relation is normally set up in the local $\bar{s}, \bar{n}$ - coordinate system, it has to be rotated to the global coordinate system. With $\boldsymbol{R}$ the rotation matrix between both coordinate systems the stiffness matrix which enters the global momentum balance reads:

$$\overline{\boldsymbol{D}_d} = \boldsymbol{R}^T \boldsymbol{D}_d \boldsymbol{R} \tag{17}$$

The flow inside the fracture is described in a similar manner as for Newtonian fluids [8]. The pressure difference over the fracture is assumed to be small compared to the pressure gradients in the surrounding porous medium. This allows the assumption of a uniform pressure in the normal direction inside the fracture. Furthermore, it is assumed that the fluid inside the fracture reacts fast to changes in the pressure compared to the fluid inside the porous media. This allows the fluid inside the fracture to be at a steady state. A schematic overview of the fracture, including the local $(\bar{s}, \bar{n})$ coordinate system and the definition of the fracture height h, is given in Figure 1.

Combining the momentum balance of the fluid in the fracture in the $\bar{s}$-direction for a two-dimensional configuration,

$$-\frac{\partial p}{\partial \bar{s}} + \frac{\partial \tau}{\partial \bar{n}} = 0 \tag{18}$$

with the constitutive relation for power-law fluids, equation 5, yields:

$$0 = -\frac{\partial p}{\partial s} + \frac{\partial}{\partial \bar{n}}\left(\mu_0 \left(\frac{\partial v}{\partial \bar{n}}\right)^n\right)$$

(19)

Herein, p is the pressure inside the fracture, equal to the pressure of the fluid at the boundary of the surrounding porous medium, and v is the tangential velocity inside the fracture. Integrating equation 19 and assuming the velocity at the walls to be equal to the velocity v_f inside the porous medium (no slip assumption) results in an expression for the fluid velocity profile inside the fracture:

$$v(\bar{n}) = \frac{n}{n+1}\mu_0^{-\frac{1}{n}}\left|\frac{\partial p}{\partial s}\right|^{\frac{1}{n}-1}\frac{\partial p}{\partial s}\left(|\bar{n}|^{\frac{1}{n}+1} - \left(\frac{h}{2}\right)^{\frac{1}{n}+1}\right) + v_f \quad \text{for} \quad -\frac{h}{2} \le \bar{n} \le \frac{h}{2}$$

(20)

Since the velocity profile only depends on the deformation and the pressure of the surrounding porous material, it can be used to describe the flow inside the fracture without adding pressure degrees of freedom. The velocity v_f at the wall is approximated from the generalised Darcy's relation inside the porous bulk material and reads:

$$v_f = -\frac{k_f^*}{n_f}\left|\frac{\partial p}{\partial s}\right|^{\frac{1}{n}-1}\frac{\partial p}{\partial s} + \dot{u}_s$$

(21)

with $\dot{u}_s$ the velocity of the solid tangential to the fracture at the wall.

We complement the constitutive relation and the momentum balance by the mass balance in the fracture:

$$\frac{\partial \rho_f}{\partial t} + \nabla \cdot \left(\rho_f v\right) = 0$$

(22)

where ρ_f is the fluid density. Since the fluid velocity inside the fracture is much higher than that inside the porous medium, the compressibility of the fluid inside the fracture can be neglected. For two-dimensional configurations this assumption reduces eq. 22 to:

$$\frac{\partial v}{\partial s} + \frac{\partial w}{\partial \bar{n}} = 0$$

(23)

where w is the velocity in the normal direction. Integrating this equation over the height of the fracture results in the velocity jump normal to the fracture:

$$[\![w]\!]_f = w\left(\frac{h}{2}\right) - w\left(-\frac{h}{2}\right) = -\int_{-\frac{h}{2}}^{\frac{h}{2}} \frac{\partial v}{\partial s}d\bar{n}$$

(24)

Substitution of the velocity for a power-law fluid from eq. 20 into this equation subsequently results in:

$$[\![w]\!]_f = \frac{2}{2n+1}\left(\frac{h}{2}\right)^{\frac{1}{n}+2}\mu_0^{-\frac{1}{n}}\left|\frac{\partial p}{\partial s}\right|^{\frac{1}{n}-1}\frac{\partial^2 p}{\partial s^2} + \left(\frac{h}{2}\right)^{\frac{1}{n}+1}\mu_0^{-\frac{1}{n}}\left|\frac{\partial p}{\partial s}\right|^{\frac{1}{n}-1}\frac{\partial h}{\partial s}\frac{\partial p}{\partial s} - h\frac{\partial v_f}{\partial s}$$

(25)

In order to relate the expression for the crack inflow/outflow to that for the fluid flow inside the porous medium, we depart from the definition for the fluid flux inside the porous material:

$$\boldsymbol{n}_{\Gamma_d} \cdot \boldsymbol{q}_d = \frac{1}{2}[\![\boldsymbol{n} \cdot \boldsymbol{q}]\!] = \frac{1}{2}n_f[\![w_f - w_s]\!]_{porous}$$

(26)

with $[\![w_s]\!]$ the velocity jump of the solid normal to the fracture and $[\![\boldsymbol{n} \cdot \boldsymbol{q}]\!]$ the fluid flux jump normal to the fracture. Next, the velocities of the solid and the fluid inside the porous medium are related to those inside the fully open fracture via:

$$[\![w_f]\!]_{porous} = \frac{1}{n_f}[\![w_f]\!]_{fracture}$$

(27)

$$[\![w_s]\!]_{porous} = \frac{1}{n_f}[\![w_s]\!]_{fracture}$$

(28)

Using these definitions and exploiting equation 26 results in the coupling between the flow inside the porous material and that inside the fracture:

$$\boldsymbol{n}_{\Gamma_d} \cdot \boldsymbol{q}_d = \frac{1}{2}\left([\![w_f]\!] - [\![w_s]\!]\right)$$

(29)

with $[\![w_f]\!]$ defined in eq. 25 and

$$[\![w_s]\!] = \frac{\partial h}{\partial t}$$

(30)

the rate at which the fracture opens. The jump in the wall velocity accounts for the fluid being absorbed into the fracture when it opens, and being re-inserted into the porous medium when it decreases.

3 | DISCRETISATION

The weak form of the momentum balance is obtained by multiplying equation 1a with the test function $\boldsymbol{\eta}$ for the displacements and using the divergence theorem. This results in:

$$\int_{\Omega} \boldsymbol{\nabla}\boldsymbol{\eta} : (\boldsymbol{\sigma}_s - \alpha p \boldsymbol{I}) d\Omega - \int_{\Gamma_d} \boldsymbol{\eta} \cdot \left(\boldsymbol{t}_d - p\boldsymbol{n}_d \right) d\Gamma = \int_{\Gamma_t} \boldsymbol{\eta} \cdot \bar{\boldsymbol{t}} \, d\Gamma \tag{31}$$

Similarly, equation 4a is transformed into a weak format by first substituting the expression for the fluid flux from equation 11, and multiplying the result by the test function for the pressure, ζ:

$$\int_{\Omega} \alpha\zeta\boldsymbol{\nabla} \cdot \dot{\boldsymbol{u}} \, d\Omega + \int_{\Omega} k_f^* \left| \boldsymbol{\nabla} p \right|^{1/n-1} \boldsymbol{\nabla}\zeta \cdot \boldsymbol{\nabla} p \, d\Omega + \int_{\Omega} \frac{1}{M} \zeta\dot{p} \, d\Omega + \int_{\Gamma_d} \zeta\boldsymbol{n}_d \cdot \boldsymbol{q}_d \, d\Gamma = - \int_{\Gamma_q} \zeta\overline{q} \, d\Gamma \tag{32}$$

Equations 31 and 32 have been discretised using traditional Lagrange shape functions, which are commonly used in finite element analysis, and also with Non-Uniform Rational B-Splines (NURBS), which have been proposed for use in IsoGeometric Analysis (IGA). To make the latter class of functions compatible with standard finite element data structures, Bézier extraction has been used[26], which allows the ensuing derivation to be carried out in a uniform manner. It has been argued that the higher-order continuity properties of NURBS are beneficial in poromechanical problems, since they allow for a straightforward satisfaction of the local mass balance at element boundaries[27,28]. In a subsequent section we will quantify this advantage for a typical poromechanical boundary value problem.

We next assemble the shape functions for the displacements of the solid in matrix $\boldsymbol{N}_s$ and those for the fluid pressure in $\boldsymbol{N}_f$:

$$\boldsymbol{u} = \sum_{e=1}^{n_{el}} \boldsymbol{N}_s^{el} \boldsymbol{u}_{el} \tag{33}$$

$$p = \sum_{e=1}^{n_{el}} \boldsymbol{N}_f^{el} \boldsymbol{p}_{el} \tag{34}$$

The standard finite element shape functions have a C^0-interelement continuity. As alluded to, NURBS can have higher-order continuity as NURBS of order p have a C^{p-1}-interelement continuity. Since the fracture inflow formulation from eq. 25 contains second derivatives of the pressure, cubic NURBS are exploited for the fluid pressure in order to obtain a continuous fracture inflow profile. This is impossible with Lagrangian interpolants. Therefore, quadratic shape functions are used since they satisfy the necessary variational requirements. In either case the strain-nodal displacement operator $\boldsymbol{B}$ is used to map the displacements onto strains at element level:

$$\boldsymbol{\varepsilon}^{el} = \boldsymbol{B}\boldsymbol{u}^{el} \tag{35}$$

In order to prevent spurious pressure oscillations, the inf-sup condition[29] imposes the necessary condition that the shape functions for the displacements are an order higher than those for the fluid pressure. In the finite element simulations, quadratic shape functions were however used for the displacements as well as for the fluid pressure. It was checked that no noticeable pressure oscillations occurred. When using NURBS, compliance with the inf-sup condition can be accomplished using p-refinement[30]. Herein, quartic shape functions have been used for the solid displacements.

We next use the interpolations for the displacements and for the fluid pressure, eqs 33 and 34, and the $\boldsymbol{B}$ matrix to discretise the weak form of the momentum balance, eq. 31. This results in:

$$\boldsymbol{f}_{ext} - \boldsymbol{f}_{int} - \boldsymbol{f}_d = 0 \tag{36}$$

with external force $\boldsymbol{f}_{ext}$ defined in a standard manner as:

$$\boldsymbol{f}_{ext} = \int_{\Gamma_t} \boldsymbol{N}_s \bar{\boldsymbol{t}} d\Gamma \tag{37}$$

The internal force which results from the bulk, $\boldsymbol{f}_{int}$, is given by:

$$\boldsymbol{f}_{int} = \int_{\Omega} \boldsymbol{B}^T \boldsymbol{\sigma}_s \, d\Omega - \int_{\Omega} \alpha \boldsymbol{B}^T \boldsymbol{m} \boldsymbol{N}_f \boldsymbol{p}^{el} \, d\Omega \tag{38}$$

with $\boldsymbol{m} = [1\ 1\ 0]^T$. The fracture is discretised using interface elements [11,28,30], and a mapping is introduced which relates the displacements at the interface Γ_d to the jump in the displacement at the interface:

$$[\![\boldsymbol{u}]\!]^{el} = \boldsymbol{N}_d \boldsymbol{u}^{el} \tag{39}$$

Use of this identity at the internal discontinuity Γ_d allows the term in the momentum balance which pertains to this discontinuity to be written as:

$$\boldsymbol{f}_d = \int_{\Gamma_d} \boldsymbol{N}_d^T \boldsymbol{R}^T \boldsymbol{D}_d \boldsymbol{R} \boldsymbol{N}_d \boldsymbol{u}^{el}\ d\Gamma - \int_{\Gamma_d} \boldsymbol{N}_d^T \boldsymbol{n}_{\Gamma_d} \boldsymbol{N}_f \boldsymbol{p}^{el}\ d\Gamma \tag{40}$$

where the linearisation of eq. 14 and the global stiffness matrix at the interface, eq. 17, have been used.

The time derivatives in the mass balance are discretised using a backward finite difference scheme with a constant time-step size of Δt. This results in the discretised form of eq. 32:

$$\boldsymbol{q}_{ext} - \boldsymbol{q}_{int} - \boldsymbol{q}_d = 0 \tag{41}$$

with the external fluid flux $\boldsymbol{q}_{ext}$ given by:

$$\boldsymbol{q}_{ext} = -\Delta t \int_{\Gamma_q} \boldsymbol{N}_f^T \overline{q} d\Gamma \tag{42}$$

while the internal fluid flux $\boldsymbol{q}_{int}$ reads:

$$\boldsymbol{q}_{int} = \int_\Omega \alpha \boldsymbol{N}_f^T \boldsymbol{m}^T \boldsymbol{B} \left(\boldsymbol{u}^{t+\Delta t} - \boldsymbol{u}^t\right)\ d\Omega + \int_\Omega \Delta t k_f^* \left|\boldsymbol{\nabla}\boldsymbol{N}_f \boldsymbol{p}^{el}\right|^{\frac{1}{n}-1} \left(\boldsymbol{\nabla}\boldsymbol{N}_f\right)^T \boldsymbol{\nabla}\boldsymbol{N}_f \boldsymbol{p}^{el}\ d\Omega + \int_\Omega \frac{1}{M} \boldsymbol{N}_f^T \boldsymbol{N}_f \left(\boldsymbol{p}^{t+\Delta t} - \boldsymbol{p}^t\right)\ d\Omega \tag{43}$$

Since the fluid fluxes at the top and bottom walls of the fracture correspond to the same pressure degrees of freedom, the fluid flux must be applied twice to the degrees of freedom. Using equation 29 with equation 30 for the fluid inflow due to fracture opening results in:

$$\boldsymbol{q}_d = \int_{\Gamma_d} 2\Delta t \boldsymbol{N}_f^T \left(\frac{1}{2}\left([\![w]\!]_f - [\![w]\!]_s\right)\right)\ d\Omega \tag{44}$$

with

$$[\![w]\!]_s = \frac{\boldsymbol{n}_{\Gamma_d} \cdot \boldsymbol{N}_d \left(\boldsymbol{u}^{t+\Delta t} - \boldsymbol{u}^t\right)}{\Delta t} \tag{45}$$

and $[\![w]\!]_f$ given by eq. 25. The pressure p and the height h of the fracture in the integration points, and their derivatives are computed according to:

$$p = \boldsymbol{N}_f \boldsymbol{p}^{el} \tag{46a}$$

$$\frac{\partial p}{\partial \overline{s}} = \boldsymbol{\nabla}\boldsymbol{N}_f \boldsymbol{p}^{el} \tag{46b}$$

$$\frac{\partial^2 p}{\partial \overline{s}^2} = \boldsymbol{\nabla}^2 \boldsymbol{N}_f \boldsymbol{p}^{el} \tag{46c}$$

$$h = \boldsymbol{n}_d \cdot \boldsymbol{N}_d \boldsymbol{u}^{el} \tag{46d}$$

$$\frac{\partial h}{\partial \overline{s}} = \boldsymbol{n}_d \cdot \boldsymbol{\nabla}\boldsymbol{N}_d \boldsymbol{u}^{el} \tag{46e}$$

$$\frac{\partial v_f}{\partial \overline{s}} = -\frac{k_f^*}{n_f n} \left|\boldsymbol{\nabla}\boldsymbol{N}_f \boldsymbol{p}^{el}\right|^{\frac{1}{n}-1} \boldsymbol{\nabla}^2 \boldsymbol{N}_f \boldsymbol{p}^{el} \tag{46f}$$

The velocity of the solid in eq. 21 has been neglected in eq. 46f since this term is assumed to be small, and its spatial gradient is likely negligible.

While all terms in eq. 36 are linear, eq. 41 contains non-linear terms. Therefore, these equations are linearised in a Newton-Raphson sense:

$$\begin{bmatrix} \boldsymbol{K} + \frac{\partial \boldsymbol{f}_d}{\partial \boldsymbol{u}} & -\boldsymbol{Q} - \frac{\partial \boldsymbol{f}_d}{\partial \boldsymbol{p}} \\ -\boldsymbol{Q}^T & -\boldsymbol{C} - \boldsymbol{H} \end{bmatrix} \begin{bmatrix} d\boldsymbol{u} \\ d\boldsymbol{p} \end{bmatrix} = \begin{bmatrix} \boldsymbol{f}_{ext} \\ -\boldsymbol{q}_{ext} \end{bmatrix} - \begin{bmatrix} \boldsymbol{f}_{int} + \boldsymbol{f}_d \\ -\left(\boldsymbol{q}_{int} + \boldsymbol{q}_d\right) \end{bmatrix} \tag{47}$$
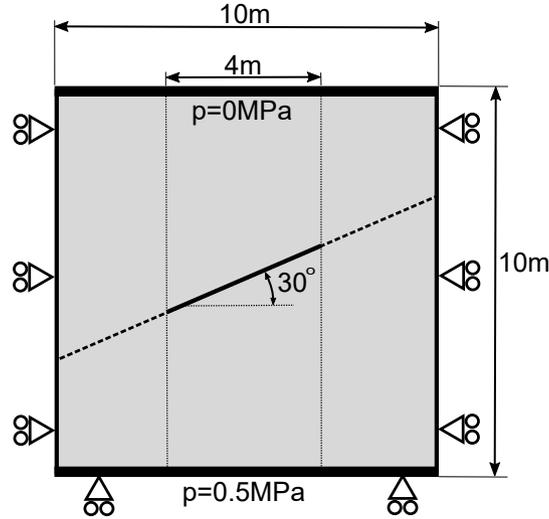
FIGURE 2 Overview of the geometry and boundary conditions.

with the sub-matrices defined as:

$$\boldsymbol{K} = \int\limits_{\Omega} \boldsymbol{B}^T \boldsymbol{D} \boldsymbol{B} \, d\Omega \tag{48a}$$

$$\boldsymbol{Q} = \int\limits_{\Omega} \alpha \boldsymbol{B}^T \boldsymbol{m} \boldsymbol{N}_f \, d\Omega \tag{48b}$$

$$\boldsymbol{C} = \int\limits_{\Omega} \frac{1}{M} \boldsymbol{N}_f^T \boldsymbol{N}_f \, d\Omega \tag{48c}$$

$$\boldsymbol{H} = \int\limits_{\Omega} \frac{\Delta t k_f^*}{n} \left| \boldsymbol{\nabla} \boldsymbol{N}_f \boldsymbol{p}^{el} \right|^{\frac{1}{n}-1} \left(\boldsymbol{\nabla} \boldsymbol{N}_f \right)^T \boldsymbol{\nabla} \boldsymbol{N}_f \, d\Omega \tag{48d}$$

$$\frac{\partial \boldsymbol{f}_d}{\partial \boldsymbol{u}} = \int\limits_{\Gamma_d} \boldsymbol{N}_d^T \boldsymbol{R}^T \boldsymbol{D}_d \boldsymbol{R} \boldsymbol{N}_d^T \, d\Gamma \tag{48e}$$

$$\frac{\partial \boldsymbol{f}_d}{\partial \boldsymbol{p}} = \int\limits_{\Gamma_d} \boldsymbol{N}_d^T \boldsymbol{n}_{\Gamma_d} \boldsymbol{N}_f \, d\Gamma \tag{48f}$$

The tangential stiffness terms which stem from the fracture flow, eq. 44, have been neglected, since they are assumed to be small and result in lengthy terms.

The changes in the displacements, $d\boldsymbol{u}$, and in the pressure, $d\boldsymbol{p}$ are added to the total displacements and the total pressure after each iteration, after which the new internal forces, fluxes, and the new tangential stiffness matrix are computed. The main difference between the equations for non-Newtonian fluids compared to those for Newtonian fluids[27], is that not only $\boldsymbol{q}_d$ is non-linear, but also the fluid diffusion matrix $\boldsymbol{H}$.

4 | SIMULATIONS FOR NON-NEWTONIAN FLUIDS

A typical boundary value problem is now used to show the effect of non-Newtonian fluids. The problem[30] consists of a square $10m \times 10m$ plate, see Figure 2. The central part contains a $4m$ fracture at a $30°$ angle. This fracture is assumed to be stationary. The bottom is constrained in the vertical direction, while the sides are contrained horizontally. A pressure difference of $0.5 MPa$ is applied between the top and bottom. It is noted that a constant pressure difference will result in a constant fracture opening, independent of the actual fluid flow through the domain.

TABLE 1 Permeability, non-Newtonian fluid index, and base viscosity

$k[m^2]$	$n[-]$	$\mu_0[mPas^n]$	$k[m^2]$	$n[-]$	$\mu_0[mPas^n]$	$k[m^2]$	$n[-]$	$\mu_0[mPas^n]$
	0.6	34.7096		0.6	20.3925		0.6	5.5011
	0.7	14.2732		0.7	9.5782		0.7	3.5853
	0.8	5.8782		0.8	4.5056		0.8	2.3402
	0.9	2.4235		0.9	2.1218		0.9	1.5291
$1 \cdot 10^{-8}$	1.0	1.0	$7 \cdot 10^{-10}$	1.0	1.0	$1 \cdot 10^{-12}$	1.0	1.0
	1.1	0.4129		1.1	0.4716		1.1	0.6544
	1.2	0.1706		1.2	0.2225		1.2	0.4284
	1.3	0.0705		1.3	0.1050		1.3	0.2806
	1.4	0.0291		1.4	0.0496		1.4	0.1838

The properties of the solid material have been taken as: Young's modulus $E = 9.0 MPa$, Poisson's ratio $\nu = 0.4$, porosity $n_f = 0.3$, Biot modulus $M = 1.0 \cdot 10^{18} MPa$, and the Biot coefficient $\alpha = 1.0$. Three different permeabilities have been used in the simulations: $k = 1.0 \cdot 10^{-8} m^2$, $k = 7.0 \cdot 10^{-10} m^2$, and $k = 1.0 \cdot 10^{-12} m^2$, see Table 1). The values for the dummy stiffness of the interface elements are $k_n = k_s = 1.0 \cdot 10^5 MPa$.

The fluid viscosity for the Newtonian case ($n = 1$) was taken as $\mu = 1 \cdot 10^{-3} Pas$. This viscosity results in a fluid flux of $0.5 m/s$, $35 mm/s$, and $0.05 mm/s$ for the cases of a high, medium and low permeability, respectively. The power-law fluid index n was varied between 0.6 and 1.4. The base viscosity μ_0 was chosen such that all cases with a non-Newtonian fluid result in the same fluid flux as for the Newtonian fluid. This was achieved using eqs 6 and 7, resulting in the following ratio between the base viscosity for the non-Newtonian fluid and the viscosity of the Newtonian fluid:

$$\frac{\mu_0^{\frac{1}{n}}}{\mu} = \frac{n}{3n+1}\left(\frac{50}{3}\right)^{\frac{1+n}{2n}} k^{\frac{1-n}{2n}} (2C)^{-\frac{1}{n}} n_f^{\frac{n-1}{2n}} \left(\frac{\Delta p}{H}\right)^{\frac{1}{n}-1} \tag{49}$$

with Δp the applied pressure difference of $0.5 MPa$ and H the height of the domain. Effectively, the Newtonian fluid is then the linearised equivalent of the non-Newtonian fluids. The resulting base viscosities are given in Table 1 as a function of the fluid index n and the permeability k.

The simulations have been carried out for fifty time steps of each $\Delta t = 1 s$, when a steady-state situation had been reached. A mesh was used composed of 80×40 Bézier elements with NURBS basis functions. As will be detailed in Section 5, this discretisation gives accurate results with respect to the displacements, pressures and the fluid velocities measured in the centre of the fracture, and gives a good approximation of the jump in velocity over the fracture. The results are presented for a steady-state situation.

Figure 3 shows the direction and magnitude of the flow inside the porous medium. To show the effect of the fracture on the fluid flux, the difference in velocity between the fractured and non-fractured results is shown in figure 4. This shows how the presence of a fracture can influence the fluid flow. Even though the magnitude of the flux difference can be different depending on the used parameter set, e.g. shear thinning or shear thickening, similar effects are observed. The fracture reinforces the fluid flow in the bottom left and top right corners, thereby increasing the total fluid flow. Since the fracture transports fluid, there is less fluid inside the porous medium tangential to the fracture. This effect of the fracture is similar for all other cases (not shown here), only the magnitude of the fluid flux varies. It is noted that the fracture opening is approximately equal for all cases due to the prescribed pressure boundary conditions.

The results for a high permeability ($k = 1 \cdot 10^{-8}$) are shown in Figure 5. The fluid velocity in the centre of the fracture, Figure 5a, shows that shear-thickening fluids have much higher velocities compared to shear-thinning and Newtonian fluids. This is also reflected in the velocity jump normal to the fracture, Figure 5b. The higher velocity inside the fracture implies that more fluid must enter and leave the fracture, thereby resulting in higher inflow velocities for the shear-thickening fluids. It is noted, however, that the outflow velocity is significantly lower than the fluid flux of $0.5 m/s$ which occurs inside the porous medium. Further, the influence of the fracture on the pressure inside the porous medium remains negligible.

Different from the results for a high permeability, for a lower value of the permeability, $k = 7 \cdot 10^{-10}$, only a small influence of the fluid index on the velocity in the centre of the fracture is observed, see Figure 6b. As a consequence, the velocity jump in Figure 6c is also less dependent on the fluid index. The slightly larger influence compared to the velocity in the centre is caused

(a) Shear-thinning fluid (n=0.6).

(b) Shear-thickening fluid (n=1.4).
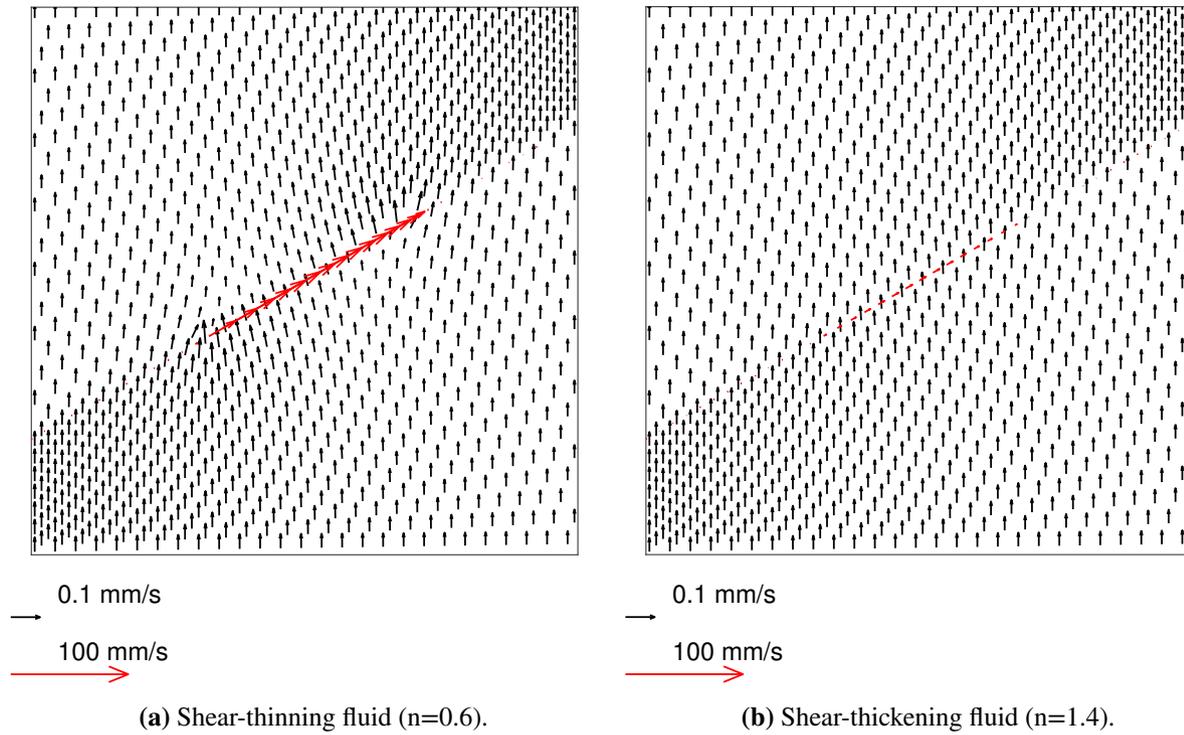
FIGURE 3 Fluid flux for the low permeability case ($k = 1 \cdot 10^{-12}$) at steady state (t=50s). Black arrows represent the fluid flux inside the porous media and red arrows represent the fluid velocity in the centre of the fracture.

(a) Shear-thinning fluid (n=0.6).

(b) Shear-thickening fluid (n=1.4).
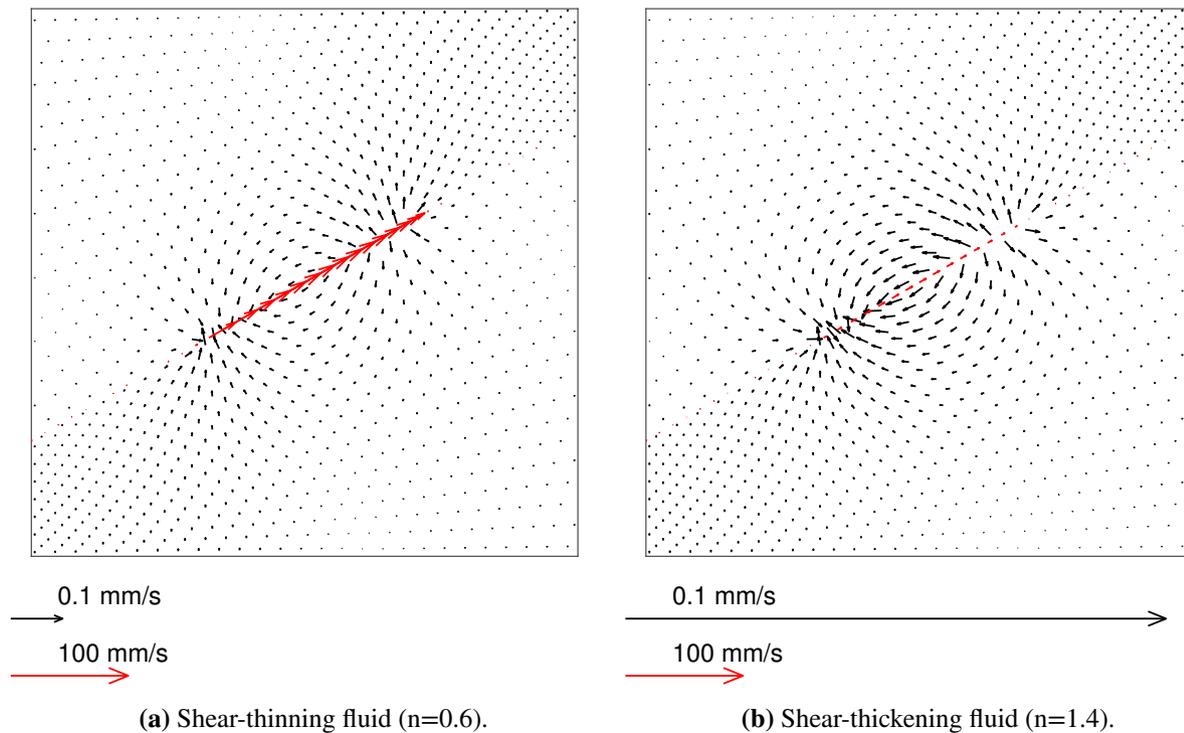
FIGURE 4 Difference in the fluid flux due to the presence of the fracture for the low permeability case ($k = 1 \cdot 10^{-12}$) at steady state (t=50s). Black arrows represent the difference in fluid flux inside the porous media and red arrows represent the fluid velocity in the centre of the fracture.

(a) Fluid velocity at the centre of the fracture

(b) Jump in velocity normal to the fracture
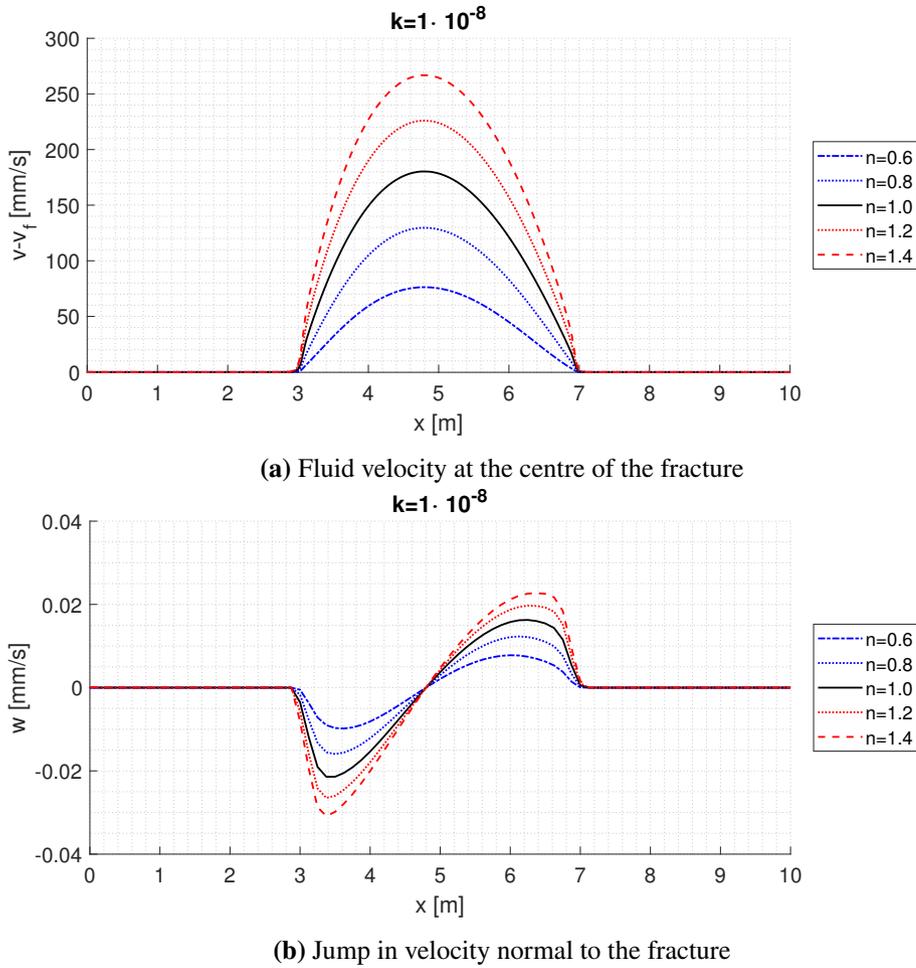
FIGURE 5 Results for $k = 1 \cdot 10^{-8} m^2$ at steady state (t=50s)

by the fact that the inflow not only depends on the maximum velocity, but also on the shape of the fluid flow profile. For shear-thinning fluids the flow profile has a shape which rather looks like a square, while shear-thickening fluids have a more triangular profile. Therefore, for a lower value of the fluid index slightly more fluid is transported compared to higher values of the fluid index fluids while the velocity at the centre has the same value. Similar to the case of a high permeability the velocity jump is small compared to the fluid flux inside the porous medium ($35mm/s$), thus limiting the influence of the fracture on the pressure inside the porous medium, see Figure 6a.

Compared to a high permeability, the fluid velocity for the simulations with $k = 1 \cdot 10^{-12}$ exhibit an inverse influence of the fluid index, see Figure 7b. Shear-thinning fluids have higher velocities compared to those computed for Newtonian fluids, while shear-thickening result in lower velocities. This is also reflected in the velocity jump normal to the fracture in Figure 7c, with a much higher inflow for shear-thinning fluids than for shear-thickening fluids. Different from the other two cases, the velocity jump normal to the fracture is of the same magnitude as the fluid flux inside the porous medium ($0.05mm/s$). Here, the imposed pressure difference causes the fracture to have a considerable influence on the pressure inside the porous medium which surrounds the fracture, see Figure 7a. For shear-thinning fluids, this influence is sufficiently large to considerably change the pressures and pressure gradients, see Figure 8. These large changes correspond to the results of Figure 4a, where the large differences indicate significant changes in the fluid pressure gradients due to the fracture.

The total fluid flux through the domain is computed by integrating the vertical flux on the top and bottom boundaries. These fluxes are used to determine the increase in fluid flow due to the presence of the fracture, as follows:

$$q_{enh} = \frac{q_{frac} - q_0}{q_0} \cdot 100\% \tag{50}$$
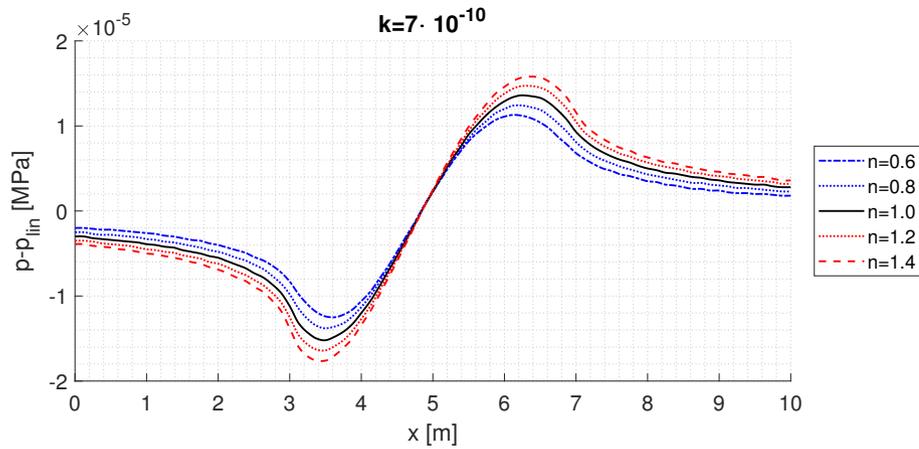
(a) Difference in pressure relative to that in the bulk along the discontinuity
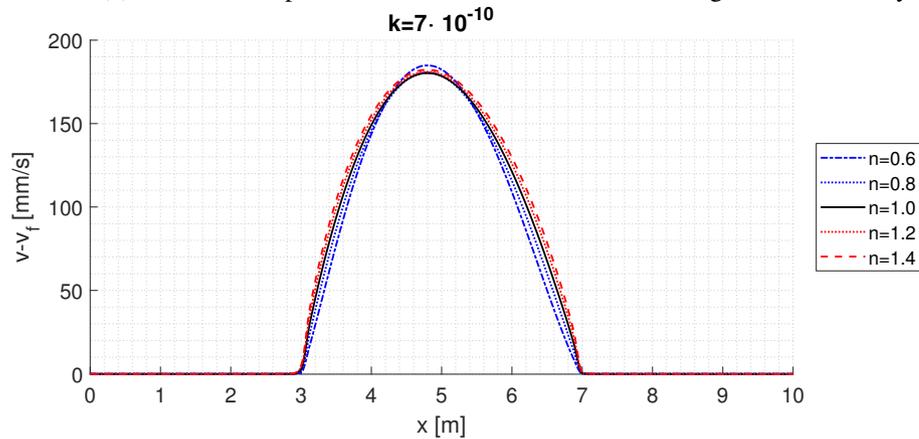
(b) Fluid velocity at the centre of the fracture
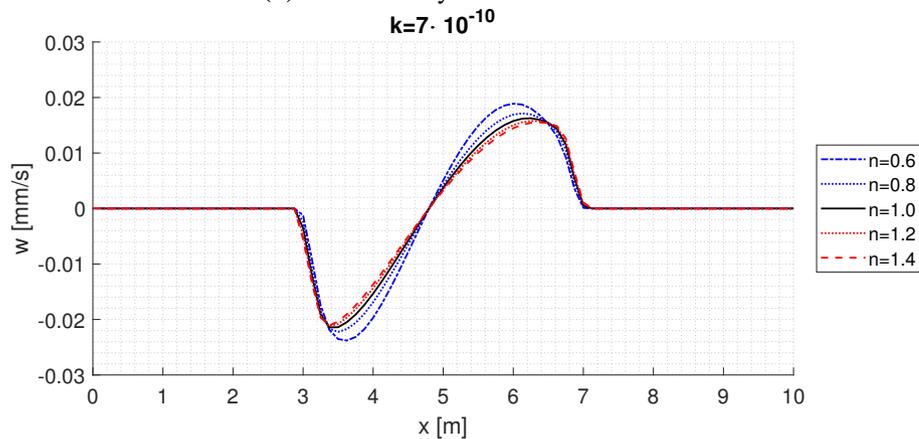
(c) Velocity jump normal to the fracture

FIGURE 6 Results for $k = 7 \cdot 10^{-10} m^2$ at steady state (t=50s)

with q_{frac} the total fluid flux calculated at the top and bottom boundaries for the case with a fracture, and q_0 for the case without. The results are shown in Figure 9. For the cases with the two higher permeabilities, the total fluid flow is not influenced markedly by the fracture. In contrast, for a low permeability the fracture causes an increase in the total fluid flow of up to 2.793% for shear-thinning fluids. While for a high permeability the fluid flow increases with an increasing value of the fluid index, the opposite occurs for a low permeability. This is consistent with the results for the flow inside the fracture, which also show this effect.

(a) Difference in pressure relative to that in the bulk along the discontinuity

(b) Fluid velocity at the centre of the fracture

(c) Jump in velocity normal to the fracture
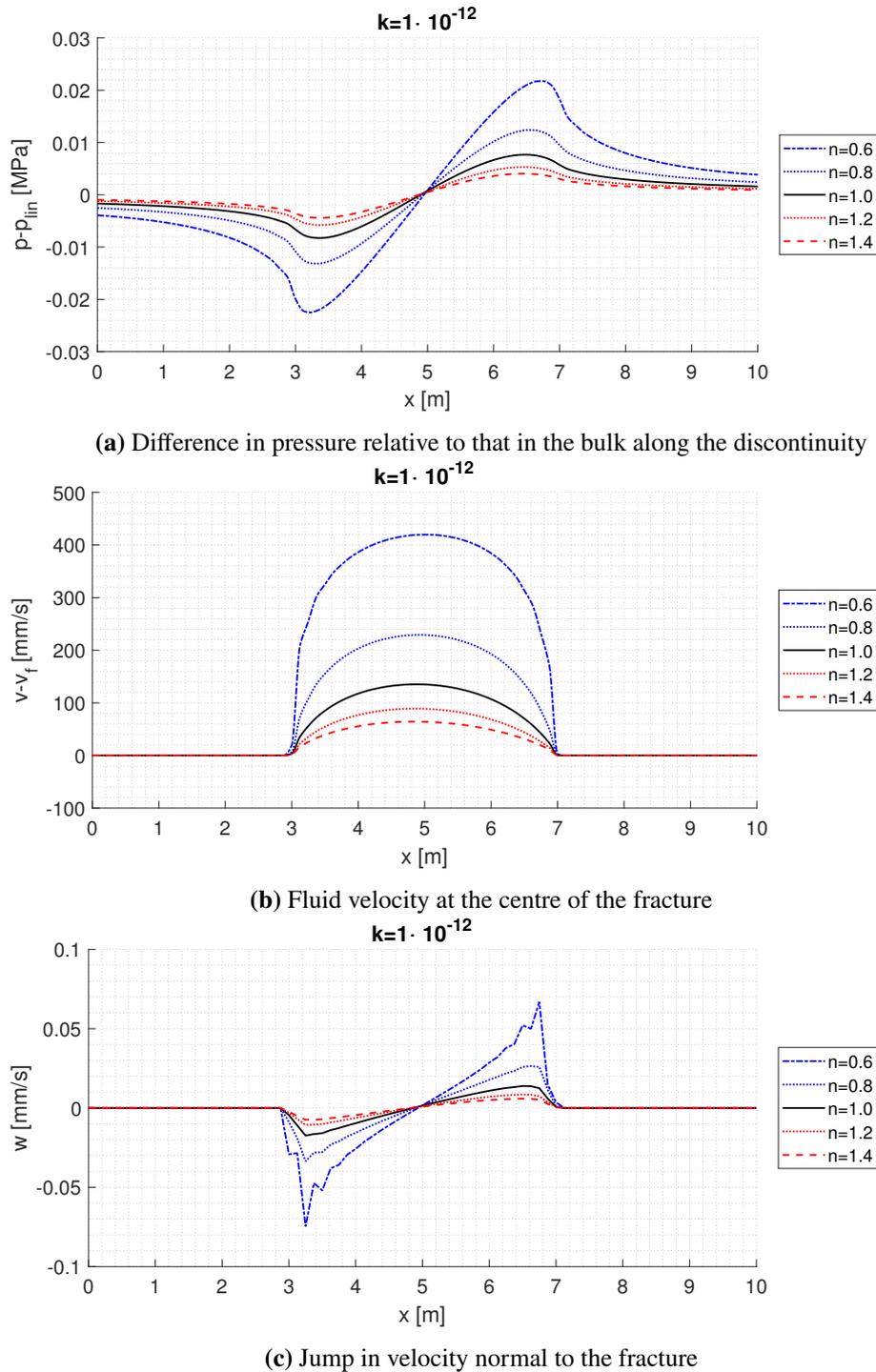
FIGURE 7 Results for $k = 1 \cdot 10^{-12} m^2$ at steady state (t=50s)

We finally note that the simulations for non-Newtonian fluids were carried out for a constant permeability and that all non-Newtonian fluids linearise to the same Newtonian fluid. Therefore, the simulations also show the effect of including the behaviour of a non-Newtonian fluid compared to linearising the fluid behaviour. It was shown for $k = 7 \cdot 10^{-10}$ that the influence on the velocity at the centre can be small. However, for low and high permeabilities, large effects were observed regarding the fluid velocity. Furthermore, these effects were mirrored, with a high velocity for shear-thickening fluids for the high permeability case, while a higher velocity was observed for a low permeability case for the shear-thinning fluid. The difference between the
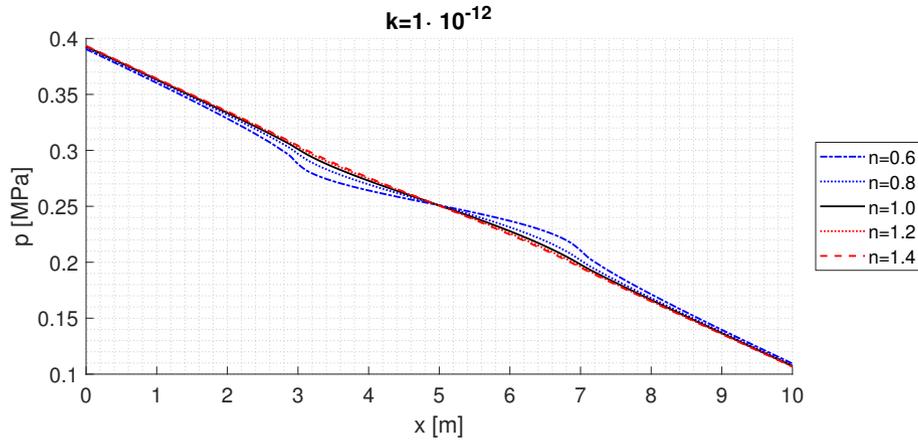
FIGURE 8 Pressure along the discontinuity
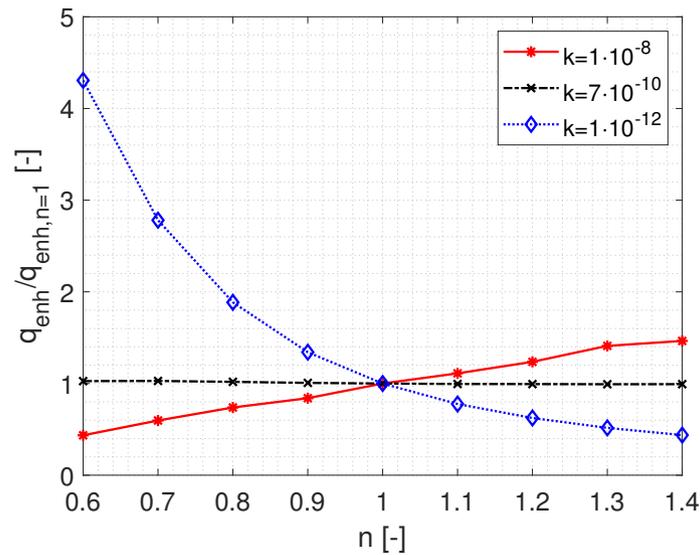
FIGURE 9 Increase in total fluid flux through the domain due to the presence of the fracture. The values have been normalised with the results for a Newtonian fluid, $q_{enh,n=1} = 7.770 \cdot 10^{-5}\%$ for $k = 1 \cdot 10^{-8} m^2$, $q_{enh,n=1} = 1.139 \cdot 10^{-3}\%$ for $k = 7 \cdot 10^{-10} m^2$ and $q_{enh,n=1} = 0.6486\%$ for $k = 1 \cdot 10^{-12} m^2$

linearised Newtonian and non-Newtonian fluids can also be observed in the total fluid flux through the domain, with increases in fluid flux between 2.793% for $n = 0.6$, while the increase for Newtonian fluids was only 0.6486% and shear-thickening fluids showed an even lower increase, down to 0.2837% for $n = 1.4$.

5 | MESH SENSITIVITY STUDY FOR NURBS BASED FINITE ELEMENTS

Simulations using different meshes were done in order to determine the required element size for obtaining accurate results regarding displacements, pressures, and the fluid velocity normal and tangential to the fracture. These simulations were done for $k = 1 \cdot 10^{-12}$, since this permeability showed the largest influence of the fracture on the pressure in the bulk material in Section 4. The upper and lower limits of fluid index, $n = 0.6$ and $n = 1.4$ respectively, were used in these simulations.

NURBS basis functions were used, with quartic shape functions for the displacements and cubic shape functions for the fluid pressure. The following Bézier extracted element meshes were used: 20×10, 40×20, 60×30, 80×40, 100×50, 120×50, 140×50, and 160×50. Only the number of elements in the horizontal direction was varied for meshes finer than 100×50, since
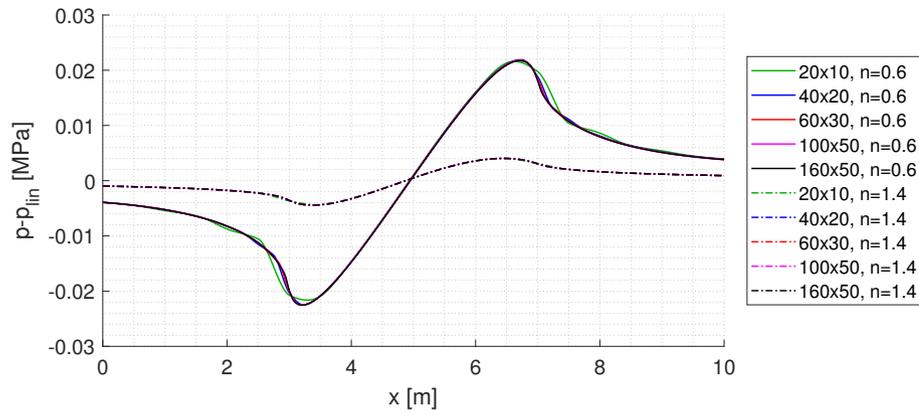
(a) Difference in pressure relative to that in the bulk along the fracture
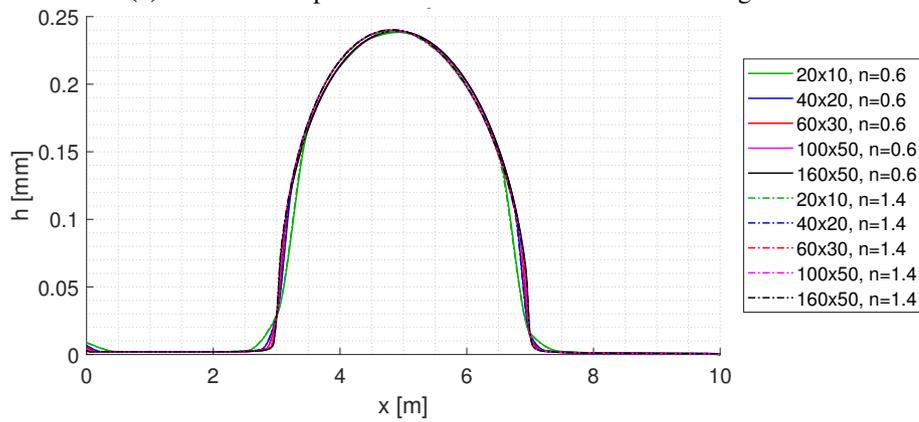
(b) Fracture opening
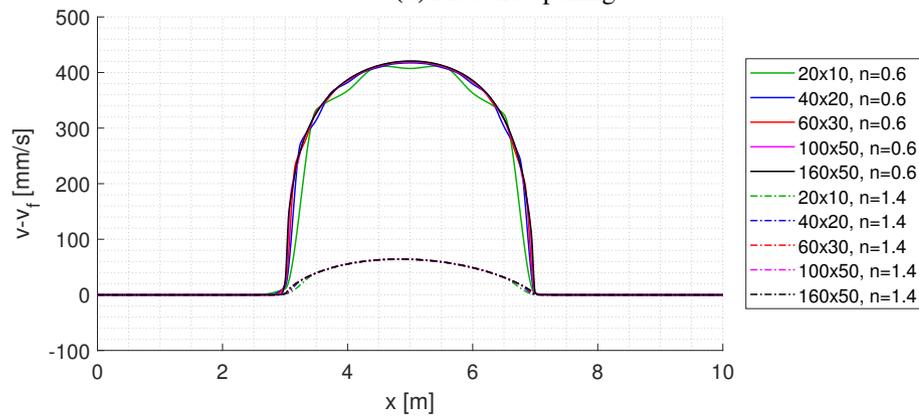
(c) Fluid velocity at the centre of the fracture

FIGURE 10 Mesh sensitivity when using NURBS shape functions. Results are shown along the discontinuity for a steady state (t=50 s) for $k = 1 \cdot 10^{-12}$.

it was assumed that 50 elements in the vertical direction was sufficient. For the sake of visibility, the results from the 80×40, 120×50 and 140×50 meshes are not shown in the figures.

The results are shown in Figure 10. The pressure distribution in Figure 10a shows only minor differences between the 20×10 and the 40×20 meshes. Further refinement of the mesh results in no visible difference compared to the 40×20 mesh. This indicates that a coarse mesh is sufficient to accurately represent the influence of the fracture on the pressure inside the bulk material.
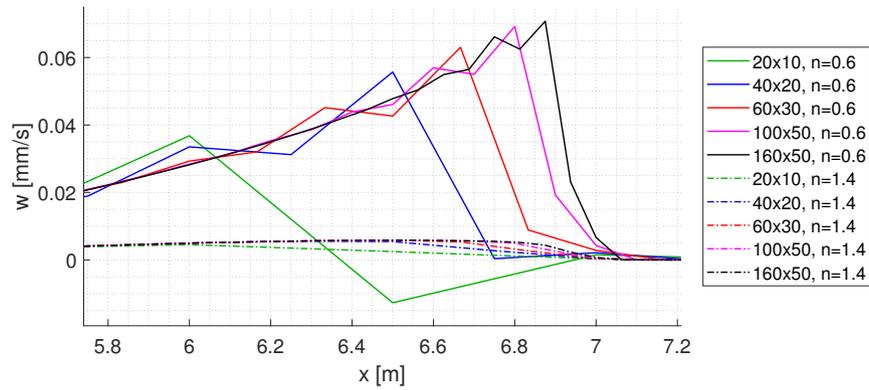
FIGURE 11 Velocity jump normal to the fracture, enlarged around the right crack tip

The fracture opening is given in Figure 10b. The centre of the graph shows similar results as the pressure: Small differences between the two coarsest meshes, and no difference for more refined meshes. Near the tips of the fracture, at $x = 3m$ and $x = 7m$, the results are more sensitive to the discretisation. This is partly due to the quartic shape functions not being able to represent a sharp fracture tip. Instead, the opening height at the tips requires approximately one non-fractured Bézier element to correctly represent a still closed fracture. While this results in visible differences in the tip aperture, it does not appear to influence the opening in the remaining part of the fracture.

The fluid velocity in the centre of the fracture, shown in Figure 10c, shows slight differences between the 40×20 and the 60×30 meshes. However, refining the mesh any further shows no visible change in the computed velocity. Since the velocity at the centre depends on the fracture opening, the results near the crack tips show a somewhat larger mesh dependence. It is somewhat less pronounced than the mesh dependence of the crack opening, since the velocity scales non-linearly with the crack opening, which reduces the effect of small differences near the tip, while it reinforces the effect of differences in the crack opening near the centre.

Figure 11 shows the velocity jump of the fluid normal to the fracture. Clearly, there is now a significant mesh dependence. Only for meshes finer than the 100×50 mesh the differences become fairly small, but close to the crack tip minor differences persist even for the two most refined meshes. From the above it transpires that when using NURBS even the coarser meshes are sufficient to accurately simulate the deformations and pressures in the porous medium. When focusing on the velocity of the fluid in the fracture, however, a finer mesh is required. Finally, really fine meshes are needed for obtaining accurate results for the fluid inflow and outflow from the fracture. However, in spite of the fact that fine meshes are needed for accurately obtaining these local flow patterns, the resulting pressure changes in the porous medium remain accurate also for considerably coarser meshes.

6 | COMPARISON WITH STANDARD FINITE ELEMENTS

The analyses of the previous section were repeated using standard finite element shape functions. Now, quadratic Lagrangian shape functions were used both for the displacements and for the fluid pressure.

The results are given in Figure 12. The pressure inside the fracture, Figure 12a, shows that differences only start to level out after the 60×30 mesh, which is different for the results that were obtained using NURBS. This corresponds to earlier observations, where it was concluded that for coarse meshes NURBS already yield the same accuracy as that obtained using Lagrangian basis functions for finer meshes [27,28]. The results for the crack opening shown in Figure 12b confirm this, but shows that now no small elements are necessary near the crack tips to obtain a zero opening. This is because standard finite elements allow for discontinuous gradients, and are therefore able to simulate sharp crack tips.

The fluid velocity in the centre of the fracture is given in Figure 12c. Due to the C^0 interelement continuity of standard finite element shape functions, jumps in the velocity profile occur since this velocity depends on pressure gradients. While the magnitude of these jumps decreases upon mesh refinement, jumps are still visible for the finest mesh. Indeed, results for the two finest meshes have not yet converged, which was different for the solutions employing NURBS.

The jump in fluid velocity normal to the fracture around the crack tips is given in Figure 13. A comparison of these results with those obtained using NURBS shows that the jump in fluid velocity near the crack tip is much higher in the standard finite

(a) Difference in pressure relative to that in the bulk along the fracture

(b) Fracture opening

(c) Fluid velocity at the centre of the fracture
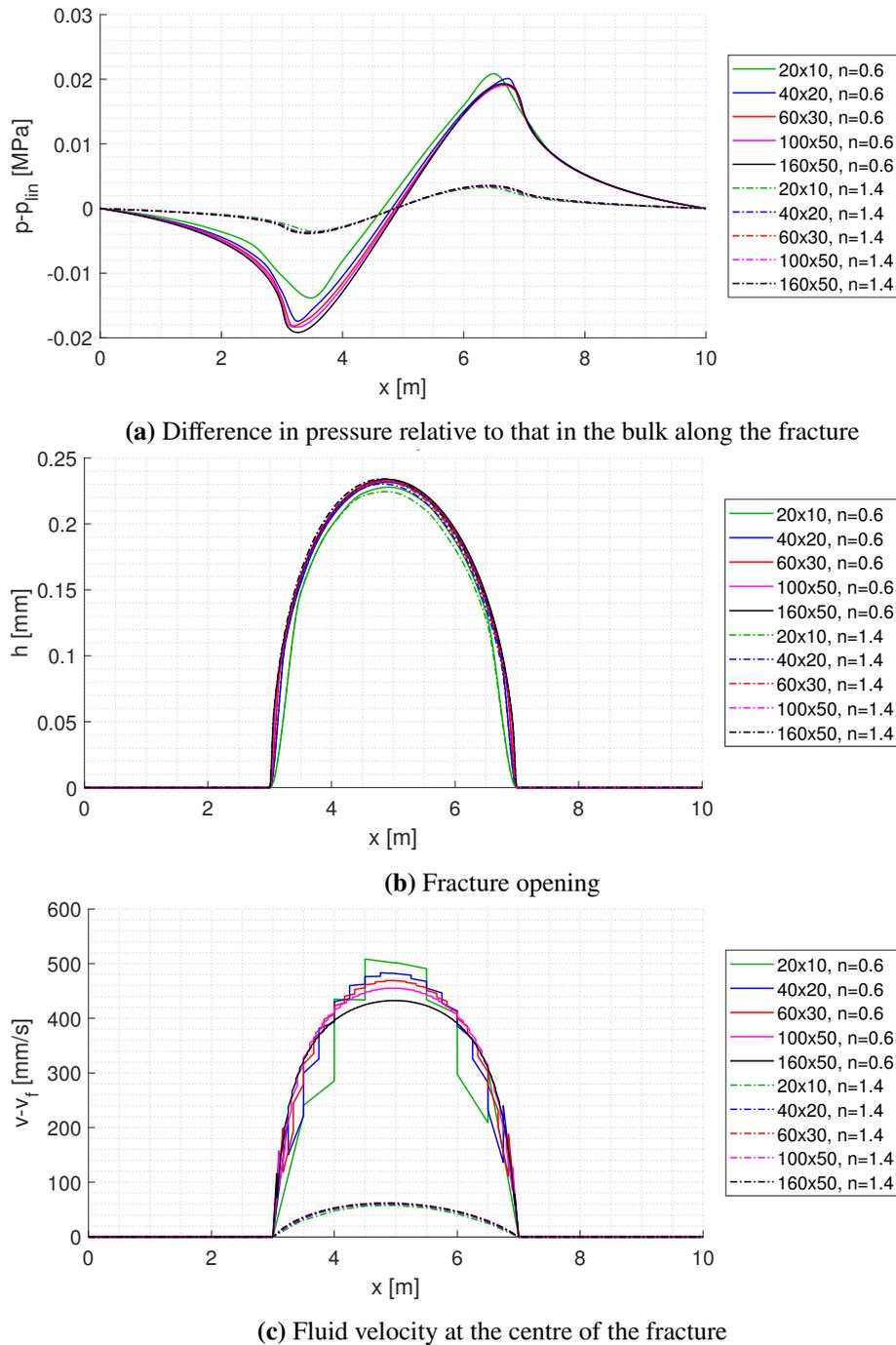
FIGURE 12 Mesh sensitivity when using standard Lagrangian shape functions. Results are shown along the discontinuity for a steady state (t=50 s) for $k = 1 \cdot 10^{-12}$.

element solutions. These higher values for the jumps are caused by the strong oscillations, which can occur because of the lack of higher-order interelement continuity of standard finite elements. Interestingly, the results tend to worsen, rather than improve, upon mesh refinement.

These results indicate that standard finite element simulations can correctly represent displacements and pressures inside the porous medium, but a finer mesh is required compared to NURBS based (isogeometric) analyses. However, standard Lagrangian shape functions cannot well reproduce local features such as the fluid velocity or the inflow at the crack tip. This is caused by the C^0 continuity of standard finite element shape functions.
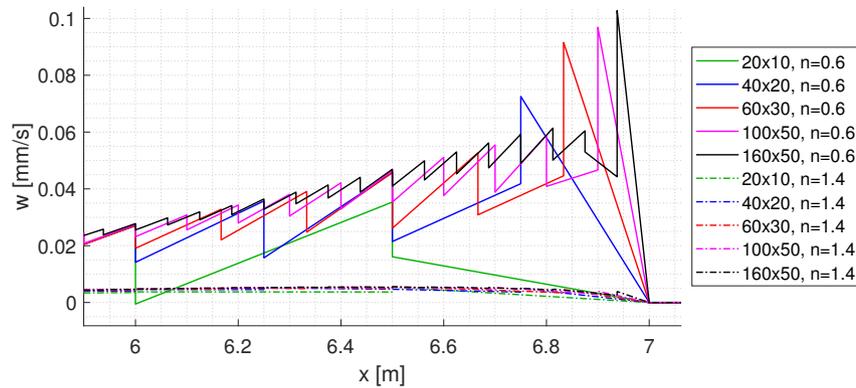
FIGURE 13 The velocity jump normal to the fracture enlarged around the right crack tip. The results have been obtained using standard finite element simulations.

7 | CONCLUDING REMARKS

A numerical model has been developed for non-Newtonian power-law fluids in deformable, fractured porous media. The model has been augmented with a sub-grid scale model for the fracture, allowing for the accurate representation of the (non-Newtonian) fluid transport inside fractures, while retaining the ability to model large domains. Discretisation has been done using standard (Lagrangian) finite element shape functions as well as using Bézier extracted NURBS shape functions, commonly used in Computer-Aided Design.

Simulations have been carried out for different values of the power-law fluid index. Depending mainly on the permeability of the porous medium that surrounds a fracture, the effects of the non-Newtonian character of a fluid are more or less pronounced. Generally, local features showed the largest differences, like the fluid velocity in the centre of the crack, or the inflow velocity at the tips. Depending on the value of the fluid index, a significant increase has also been observed of the effect of the fracture on the total fluid transport through the domain.

Results from a mesh sensitivity study show that a coarse discretisation with NURBS is already capable of accurately simulating the fluid transport in the fracture including its effect on the pressure and deformations in the surrounding porous material. Standard finite elements can also do this, but need some more refinement to attain the same level of accuracy. However, the local fluid velocity normal and tangential to the fracture could only be simulated accurately using NURBS, since the lower interelement continuity of standard finite elements cause severe jumps in the velocity profile, resulting in a severe overshoot.

References

1. Boone TJ, Ingraffea AR. A numerical procedure for simulation of hydraulically-driven fracture propagation in poroelastic media. *International Journal for Numerical and Analytical Methods in Geomechanics* 1990; 14(1): 27–47.

2. Segura JM, Carol I. Coupled HM analysis using zero-thickness interface elements with double nodes. Part I: Theoretical model. *International Journal for Numerical and Analytical Methods in Geomechanics* 2008; 32: 2083–2101.

3. Segura JM, Carol I. Coupled HM analysis using zero-thickness interface elements with double nodes. Part II: Verification and application. *International Journal for Numerical and Analytical Methods in Geomechanics* 2008; 32: 2103–2123.

4. Schrefler BA, Secchi S, Simoni L. On adaptive refinement techniques in multifield problems including cohesive fracture. *Computer Methods in Applied Mechanics and Engineering* 2006; 195: 444–461.

5. Secchi S, Simoni L, Schrefler BA. Mesh adaptation and transfer schemes for discrete fracture propagation in porous materials. *International Journal for Numerical and Analytical Methods in Geomechanics* 2007; 31: 331–345.

6. de Borst R, Réthoré J, Abellan MA. A numerical approach for arbitrary cracks in a fluid-saturated medium. *Archive of Applied Mechanics* 2006; 75(10-12): 595–606.

7. Réthoré J, de Borst R, Abellan MA. A discrete model for the dynamic propagation of shear bands in a fluid-saturated medium. *International Journal for Numerical and Analytical Methods in Geomechanics* 2007; 31: 347–370.

8. Réthoré J, de Borst R, Abellan MA. A two-scale approach for fluid flow in fractured porous media. *International Journal for Numerical Methods in Engineering* 2006; 71(7): 780–800.

9. Remij EW, Remmers JJC, Huyghe JM, Smeulders DMJ. The enhanced local pressure model for the accurate analysis of fluid pressure driven fracture in porous materials. *Computer Methods in Applied Mechanics and Engineering* 2015; 286: 293–312.

10. de Borst R. Fluid flow in fractured and fracturing porous media: A unified view. *Mechanics Research Communications* 2017; 80: 47–57.

11. de Borst R. *Computational Methods for Fracture in Porous Media*. Amsterdam - Oxford - Cambridge: Elsevier . 2018.

12. Mohammadnejad T, Khoei AR. Hydro-mechanical modeling of cohesive crack propagation in multiphase porous media using the extended finite element method. *International Journal for Numerical and Analytical Methods in Geomechanics* 2013; 37(10): 1247–1279.

13. Mohammadnejad T, Khoei AR. An extended finite element method for hydraulic fracture propagation in deformable porous media with the cohesive crack model. *Finite Elements in Analysis and Design* 2013; 73: 77–95.

14. Khoei AR, Vahab M, Haghighat E, Moallemi S. A mesh-independent finite element formulation for modeling crack growth in saturated porous media based on an enriched-FEM technique. *International Journal of Fracture* 2014; 188(1): 79–108.

15. Di Federico V, Pinelli M, Ugarelli R. Estimates of effective permeability for non-Newtonian fluid flow in randomly heterogeneous porous media. *Stochastic Environmental Research and Risk Assessment* 2010; 24(7): 1067–1076.

16. Morais AF, Seybold H, Herrmann HJ, Andrade JS. Non-Newtonian fluid flow through three-dimensional disordered porous media. *Physical Review Letters* 2009; 103(19): 194502.

17. Lavrov A. Numerical modeling of steady-state flow of a non-Newtonian power-law fluid in a rough-walled fracture. *Computers and Geotechnics* 2013; 50: 101–109.

18. Lavrov A. Redirection and channelization of power-law fluid flow in a rough-walled fracture. *Chemical Engineering Science* 2013; 99: 81–88.

19. Bao K, Lavrov A, Nilsen HM. Numerical modeling of non-Newtonian fluid flow in fractures and porous media. *Computational Geosciences* 2017; 21(5-6): 1313–1324.

20. Christopher RH, Middleman S. Power-Law Flow through a Packed Tube. *Industrial & Engineering Chemistry Fundamentals* 1965; 4(4): 422–426.

21. Pascal H. Nonsteady flow of non-Newtonian fluids through a porous medium. *International Journal of Engineering Science* 1983; 21(3): 199–210.

22. Al-Fariss T, Pinder KL. Flow through porous media of a shear-thinning liquid with yield stress. *The Canadian Journal of Chemical Engineering* 1987; 65(3): 391–405.

23. Shenoy AV. Non-Newtonian Fluid Heat Transfer in Porous Media. *Advances in Heat Transfer* 1994; 24: 101–190.

24. Weisstein EW. Geometric Series. From MathWorld–A Wolfram Web Resource. http://mathworld.wolfram.com/GeometricSeries.html. .

25. de Borst R. Numerical aspects of cohesive-zone models. *Engineering Fracture Mechanics* 2003; 70(14): 1743–1757.

26. Borden MJ, Scott MA, Evans JA, Hughes TJR. Isogeometric finite element data structures based on Bézier extraction of NURBS. *International Journal for Numerical Methods in Engineering* 2011; 87(1-5): 15–47.

27. Irzal F, Remmers JJC, Verhoosel CV, de Borst R. Isogeometric finite element analysis of poroelasticity. *International Journal for Numerical and Analytical Methods in Geomechanics* 2013; 37: 1891–1907.

28. Irzal F, Remmers JJC, Verhoosel CV, de Borst R. An isogeometric analysis Bézier interface element for mechanical and poromechanical fracture problems. *International Journal for Numerical Methods in Engineering* 2014; 97(8): 608–628.

29. Chapelle D, Bathe KJ. The inf-sup test. *Computers & Structures* 1993; 47(4-5): 537–545.

30. Vignollet J, May S, de Borst R. Isogeometric analysis of fluid-saturated porous media including flow in the cracks. *International Journal for Numerical Methods in Engineering* 2016; 108(9): 990–1006.